



PAPER

[View Article Online](#)
[View Journal](#) | [View Issue](#)Cite this: *Dalton Trans.*, 2025, **54**, 8483Blue-light hydrogen production via CdS/g-C₃N₄ heterojunctions†Karen Valencia G., Agileo Hernández-Gordillo,  * Lorena Cerezo and Sandra E. Rodil 

This study introduced advanced photocatalytic heterojunctions by integrating CdS nanofibers with defect-rich polymeric carbon nitride (g-C₃N₄-V₀). Two g-C₃N₄-V₀ variants (**CN1** and **CN2**) with varying nitrogen vacancy concentrations were synthesized, which enhanced visible and near-infrared light absorption. Eight heterojunctions with different **CN1** and **CN2** contents (5–20 wt%) were prepared and tested for the hydrogen evolution reaction (HER) in ethanol–water solutions without a Pt co-catalyst. Under optimized conditions (photocatalyst mass: 0.0125 g L^{−1}, light intensity: 10 mW cm^{−2}), the **CS/CN1-15** and **CS/CN2-10** heterojunctions achieved HER rate of 4.43 and 5.25 mmol h^{−1} g^{−1}, respectively—doubling the efficiency of comparable systems. Their superior performance was attributed to enhanced light absorption, efficient charge separation, and reduced charge transfer resistance. The **CS/CN2-10** heterojunction also demonstrated long-term stability, emphasizing its promise for sustainable hydrogen production.

Received 23rd January 2025,

Accepted 16th April 2025

DOI: 10.1039/d5dt00187k

rsc.li/dalton

Introduction

Fossil fuel-based conventional energy sources significantly contribute to greenhouse gas emissions, adding to the current climate crisis. Energy transition innovations, such as the one presented in this research, are crucial in combatting climate change and fulfilling sustainable development goals.¹ Hydrogen (H₂) emerges as a clean fuel alternative, as its combustion produces only water vapor. One promising method for producing hydrogen involves the photocatalytic activation of semiconductor materials in alcohol–water solutions,² ideally utilizing solar energy. During the process, energetic photons absorbed by the semiconductor excite charge carriers, generating electron–hole pairs to drive the H⁺/H₂ reduction reaction. Extensive research has demonstrated that the efficiency of the semiconductor to promote energy conversion is limited by two types the factors: extrinsic and intrinsic. To address the extrinsic factor, attention needs to be paid to improving the charge transport efficiency. In contrast, the intrinsic factor is related to its morphology, surface area, narrow absorption range within the electromagnetic spectrum, and particularly to crystal defects, which can cause electron–hole pair (e[−]/h⁺)

recombination within the bulk material, negatively affecting its photocatalytic efficiency.^{3–5}

In relation to the optical absorption aspect, many wide-bandgap semiconductors, such as TiO₂, ZnO, and ZnS, have demonstrated their effectiveness in hydrogen production through water-splitting under UV light. However, since UV radiation accounts for only about 4% of the solar spectrum, there is a growing focus on visible-light semiconductors to utilize the entire solar spectrum. Polymeric graphitic carbon nitride (g-C₃N₄) and cadmium sulfide (CdS) are promising candidates as visible-light-absorbing semiconductors for photo-induced conversion processes. Both materials can promote the H⁺/H₂ reduction reaction, as the potential energy of the photo-generated holes is more negative than the redox potential of E°(H⁺/H₂) = −0.41 V (ENH, at pH 7).⁶ Hexagonal CdS is a direct band gap semiconductor (E_g = 2.4 eV) widely used in solar cells, light-emitting diodes, device lasers and photocatalysts.^{7–9} However, it presents rapid recombination of the photogenerated charge carriers both in the bulk and on the surface, as well as limited acid resistance.¹⁰ On the other hand, graphitic g-C₃N₄ is a promising visible-light semiconductor that is non-toxic and chemically stable against acids, alkalis, and organic solvents. g-C₃N₄ is a semiconductor with an n-type character, an indirect band gap of 2.7 eV, and a two-dimensional (2D) layered structure.^{11–13} As a major challenge, it faces a high recombination rate of electron–hole pairs (e[−]/h⁺) and low absorption towards the visible–IR region, limiting its solar photocatalytic efficiency.^{11,12}

Instituto de Investigaciones en Materiales, Universidad Nacional Autónoma de México, Circuito Exterior S/N, Ciudad Universitaria, Coyoacán. C.P. 04510, Mexico City, Mexico. E-mail: agileohg@materiales.unam.mx

† Electronic supplementary information (ESI) available. See DOI: <https://doi.org/10.1039/d5dt00187k>

Regarding the intrinsic aspects of semiconductor materials, research suggests that the most effective strategy to enhance their photocatalytic activity is the modification of crystal defects or surface vacancies, aimed at reducing e^-/h^+ recombination. This can be achieved through the combination of two or more semiconductors with dissimilar band structures to form a heterojunction, thereby extending the lifetime of excitons (e^-/h^+). Heterojunctions can lead to band bending and the production of an inner electric field, which facilitates the spatial separation of the photogenerated carriers.^{14,15} Therefore, heterojunction materials, depending on the properties of the combined materials, can enhance light absorption in the visible range and reduce the recombination of electron–hole pairs.

Heterojunctions based on the CdS/g-C₃N₄ combination for photocatalytic degradation of organic molecules and for H₂ production have been the subject of extensive research, with more than 200 articles published in the last 5 years. The coupling of metal sulfides (ZnS, NiS or CdS) with g-C₃N₄ is particularly attractive because charge separation with prolonged lifetimes²⁵ has been demonstrated to have positive consequences for the photocatalytic generation of hydrogen. Such improvements can be seen in the brief literature review on hydrogen production using CdS/g-C₃N₄ composites presented in Table 1. For a detailed comparative analysis, the maximum hydrogen evolution reaction (HER) rate, defined as the normalized amount of hydrogen produced per unit time and per gram of photocatalyst, are reported. Table 1 demonstrates that for pristine CdS/g-C₃N₄ composites without adding Pt as a co-catalyst, the HER rate is between 0.5 and 2.24 mmol h^{−1} g^{−1}. While composites including Pt significantly enhance the HER rate (up to 7.75 mmol h^{−1} g^{−1}), they also substantially raise costs due to the use of a noble metal. The materials' price and the input energy cost should be considered to make the hydrogen production process sustainable. The studies shown in Table 1 typically employed, without any explanation, high photocatalyst mass loads (0.1 to 0.5 g L^{−1}) and powerful Xe lamps

(300 W) of high irradiances typically above 144–300 mW cm^{−2}.^{26,27} Most likely, high-intensity lamps are required since the water solution is saturated with a high photocatalyst load, leading to the loss of incoming light through scattering, which represents a waste of supplied energy.

In this work, we propose the evaluation of photocatalytic hydrogen production using the CdS/g-C₃N₄ composite but under energetically optimized conditions in terms of mass load vs. light intensity to further demonstrate the advantages of the intrinsic properties of the heterojunction. Our g-C₃N₄ material was synthesized using a route that allows the production of defect-rich g-C₃N₄ during the polymerization of urea by adding different percentages of hydrazine.²⁸ The advantage of the modified g-C₃N₄ (g-C₃N₄-V₀) is extended visible-IR absorption at lower energies and reduced radiative recombination of electron–hole pairs. Then, the micro g-C₃N₄-V₀ flakes were used as a support or template for the growth of CdS nanofibers *via* a solvothermal method.

The content of g-C₃N₄-V₀ was varied in the 5 to 20 wt% range, and the resulting composite photocatalysts were characterized using X-ray diffraction (XRD), Fourier transform infrared spectroscopy (FTIR), scanning electron microscopy (SEM), UV-vis diffuse reflectance spectroscopy (UV-vis DRS) and PL spectroscopy. The photocatalytic activity of the CdS/g-C₃N₄-V₀ composite was evaluated for hydrogen production in an optimized low-photocatalyst-load suspension under high blue light penetration (slightly turbid and reduced scattering light). The results indicated a twofold increase in the hydrogen production rate compared to pristine CdS nanofibers. This increase is explained by effective charge separation, stemming from the strong interaction between CdS nanofibers and the g-C₃N₄-V₀ micro-flakes, and a reduction in the electron transfer resistance, as confirmed by electrochemical impedance spectroscopy (EIS) analysis. The increased hydrogen production rate under blue light was also associated with the extended optical absorption of the CdS/g-C₃N₄-V₀ composite in the blue spectrum, related to nitrogen vacancies. A detailed analysis of

Table 1 Studies on the synthesis of CdS/g-C₃N₄ composites for hydrogen production

Contents of C ₃ N ₄ (wt%)	Sacrificial agent	300 W Xe lamp (cut off)	Mass load (g L ^{−1})	HER rate (mmol g ^{−1} h ^{−1})	Increase (relative to)	Ref.
CdS/g-C₃N₄ composites						
5, 7.5, 10, 12.5 and 15	Lactic acid (10 mL)	(≥420 nm)	0.428	1.80	—	2021 ¹⁶
10, 20, 30 and 40	Na ₂ S (0.1 M)	(≥400 nm)	0.125	2.12	36.5 to CdS	2022 ¹⁷
	Na ₂ SO ₃ (0.1 M)				36.5 to C ₃ N ₄	
33 and 25	Triethanolamine (30 mL)	Solar simulator	0.100	2.24	3.3 to CdS	2020 ¹⁸
					3.7 to C ₃ N ₄	
—	Na ₂ S (0.35 M) and Na ₂ SO ₃ (0.25 M)	(>400 nm)	0.500	0.53	12.6 to CdS	2021 ¹⁹
41	Na ₂ S-Na ₂ SO ₃ (0.25 M)	(>420 nm)	0.0625	15.3	3.8 to CdS	2019 ²⁰
					3.0 to C ₃ N ₄	
10 or 15	Ethanol (100 mL)	9 LED (454 nm)	0.025	5.25	2.0 to CdS	This work
CdS/g-C₃N₄ composites containing Pt						
20	Na ₂ S/Na ₂ SO ₃ + 3 wt% Pt	(>400 nm)	0.125	1.70	—	2022 ²¹
95, 97 and 99	Lactic acid + 3 wt% Pt	(>400 nm)	0.270	3.37	3.8 to C ₃ N ₄	2022 ²²
—	20% triethanolamine + 0.2 wt% Pt	(>400 nm)	0.100	5.40	4.0 to C ₃ N ₄	2019 ²³
97, 88, 84, 80 and 77	Lactic acid + 1 wt% Pt	(>420 nm)	0.200	7.75	5.8 to C ₃ N ₄	2019 ²⁴

The total intensity of Xe lamp is about 144–300 mW cm^{−2}. The measured blue intensity of the LED lamp is 10 mW cm^{−2}.

the reused composite recovered after the cycles was also included.

Experimental methods

Polymerization of g-C₃N₄

The graphitic g-C₃N₄-V₀ sample was prepared by heat polymerization using urea (CO(NH₂)₂, JT Baker, 99.5%) as the precursor in the presence of hydrazine hydrate (N₂H₄, Sigma Aldrich, 25 vol%) as the *in situ* modifying agent. The amount of hydrazine induces the formation of defective g-C₃N₄-V₀, as evidenced by enhanced optical absorption, following the methodology previously reported.²⁸ The procedure consisted of melting 5 g of urea for 30 minutes. Then, the molten urea powder was placed in a ceramic-covered crucible and homogeneously mixed with 1 or 2 mL of hydrazine. The impregnated hydrazine–urea powder was placed in a tubular muffle furnace and annealed at 550 °C (5 °C min^{−1} ramp) in static air for 2 h. Two hydrazine conditions were selected, labeled **CN1** (1 mL of hydrazine) and **CN2** (2 mL of hydrazine), which might reflect different fractions of defects.

Preparation of CdS nanofibers using the solvothermal method

CdS nanofibers were prepared using the solvothermal method in a mixture of solvents (water:butanol:ethylenediamine), with cadmium nitrate tetrahydrate (Cd(NO₃)₂·4H₂O, Sigma Aldrich, 98%) and carbon disulfide (CS₂, Merck, 37%) as precursor sources, employing the methodology described in ref. 29. The procedure involved preparing a Cd-complex solution by dissolving 2.1 g of cadmium salt precursor in 10 mL of distilled water. Afterward, 28 mL of butanol (BtOH, Meyer, 99.4%) was added under stirring. Subsequently, 60 mL of ethylenediamine (EN, Sigma Aldrich, 99%) was added dropwise and stirred for 10 min. Then, 2 mL of butanol containing 0.4 mL of CS₂ was added to the Cd-complex solution to avoid a violent reaction. The homogeneous solution was transferred to a Teflon reactor of 200 mL capacity, sealed and heated at 90 °C for 2 h on a magnetic grill. After that, it was allowed to cool gradually to room temperature. The resulting yellow powder was filtered, washed with water–ethanol (50/50 vol%), and dried at room temperature (RT) overnight. The dried yellow powder was labeled as **CS**.

CdS nanofiber growth on g-C₃N₄ (CS/CNX)

An *in situ* solvothermal process was used to grow CdS using g-C₃N₄-V₀ as a support, employing two steps (Fig. S1†). In the *first step*, the desired amount (5, 10, 15, or 20 wt%) of the polymerized g-C₃N₄-V₀ (**CN1** or **CN2**) powder was added into the vessel containing 28 mL of butanol (BtOH), and the suspension was subjected to sonication for 8 h to achieve complete dispersion. Simultaneously, in a Teflon reactor, 2.1 g of cadmium salt precursor was dissolved in 10 mL of distilled water, and then, 60 mL of EN was added dropwise and stirred for 10 min to prepare the Cd-complex solution. In the *second step*, the sonicated suspension was added to the Teflon reactor

containing the Cd-complex solution, and then, 2 mL of BtOH containing 0.4 mL of CS₂ was also added (Fig. S1†). The Teflon reactor was sealed and heated at 90 °C for 2 h to allow the “*in situ*” growth of CdS on g-C₃N₄-V₀. After cooling to RT, the powder composite sample was filtered, washed, and dried at RT. Samples were labeled as **CS/CNX-Y**, where *X* = 1 or 2 represents the **CN1** or **CN2** sample, and *Y* represents the amount of polymerized g-C₃N₄-V₀ (5, 10, 15 and 20 wt%).

Characterization of the CS/CNX-Y samples

The **CNX**, **CS** and **CS/CNX-Y** samples were characterized by X-ray diffraction (XRD) using a Rigaku instrument with a Cu K α radiation of 0.154 nm (50 kV, 40 mA) and a scanning interval between 10 and 60° (2 theta) with a step size of 0.05° s^{−1}. Fourier transform infrared (FTIR) absorption spectra were recorded on a Thermo Scientific Nicolet 6700 spectrometer equipped with an ATR accessory and a diamond crystal. The pressure used was 815 Psi at room temperature, and 68 scans were performed at a resolution of 4 cm^{−1} in the range of 500 and 3500 cm^{−1} in transmission mode. The morphology of the samples was analyzed by scanning electron microscopy (SEM) using a JEOL 7600F at 5 kV. The specific surface area was determined using the BET method from nitrogen adsorption–desorption isotherms at 77.4 K. The analysis was performed using a Quantachrome Autosorb instrument. Before the measurements, the samples were degassed at 120 °C under vacuum for 12 h. UV-vis diffuse reflectance spectra (DRS) were acquired on a Shimadzu 2600 spectrophotometer equipped with an ISR 2600 integrating sphere in the range of 350 to 700 nm. Barium sulfate (BaSO₄) was used as a reference blank. Absorbance spectra were recorded, and *E_g* was calculated using the Kubelka–Munk model, considering a direct transition for the CdS/g-C₃N₄ material,³⁰ extrapolating the linear part of (*F(R)* × *hν*)² versus *hν* curves to *F(R)*. Photoluminescence (PL) spectra were recorded using an Edinburgh Instruments FS5 fluorimeter with a 150 W, CW ozone-free xenon arc lamp.

Photocatalytic evaluation of CS/CNX-Y suspensions

Prior to the photocatalytic test, irradiance data were collected as a function of photocatalyst mass load to ensure high blue light penetration within the dispersed suspension and to optimize energy consumption during the photocatalytic evaluation. For this purpose, suspensions of **CS/CNX-Y** from 0.01 to 0.1 g L^{−1} were prepared and dispersed by sonication for 3 minutes. The light intensity (irradiance) of a blue LED lamp was measured as a function of the photocatalyst concentration (g L^{−1}), placing the photometer at 5 cm after the light had passed through the dispersed suspension (shown in Fig. S2†). The photometer was an SRI-2000 Spectral Light Meter, Allied Scientific Pro. The evaluation of the amount of H₂ produced by the composite photocatalyst was carried out in a 250 mL glass photoreactor. For the test, the optimal mass-load (5 mg), as determined from the previous irradiance experiments, **CNX**, **CS** or the composite photocatalyst (**CS/CNX-Y**) was added into 200 mL of ethanol–water solution (50 : 50 vol%) to form a dispersed suspension (equivalent to 0.025 g L^{−1}). The photo-

reactor containing the suspension was connected to the reaction system and purged with N_2 to displace oxygen from the system. After 1 h, the glass reactor was submerged in a water bath to maintain a constant temperature of around 34 ± 1 °C. Then, the photoreactor was irradiated with blue light from 9 blue LED lamps, each with 3 W power, radially distributed. These lamps were positioned around the glass reactor at 5 cm. The photoreactor system was coupled to a Shimadzu GC-2014 gas chromatograph equipped with a TCD detector (operating at 100 °C) and using N_2 as the carrier gas. Gas injections into the chromatograph were conducted using a peristaltic pump, performed hourly for 6 hours, and the produced H_2 was quantified using a calibration curve. An additional photocatalytic H_2 production test was performed using a physical mixture of CdS and $g-C_3N_4$, with 15% and 10 wt% of **CN1** and **CN2**.

Photoelectrochemical analysis of the thin films

Photocatalyst electrode thin films over FTO substrates were produced to perform the electrochemical evaluation under dark and blue illumination. The electrode thin films (**CS**, **CNX**, **CS/CN1-15**, and **CS/CN2-10** samples) were prepared using the spin-coating method, following a methodology previously reported.³¹ A suspension containing the synthesized sample was prepared using 50 mg of the powder in 5 mL of ethanol with 200 μ L of Nafion perfluorinated resin solution (Aldrich 80% by weight), and each suspension was sonicated for 3 h to ensure dispersion. Fluorine tin oxide-coated substrates (FTO, Aldrich, surface resistivity $\sim 7 \Omega \text{ sq}^{-1}$) were cut to dimensions of 1×1.5 cm and pre-cleaned with isopropanol/acetone/ethanol. Subsequently, 300 μ L of the dispersed powder suspension was deposited on the FTO substrate at 1500 rpm. The deposited electrode film was dried at 50 °C for 30 min, and the area of study was delimited to 0.5×0.5 cm using an insulating silicone mask. Then, photoelectrochemical measurements were performed in a conventional three-electrode cell, using an Ag/AgCl/0.1 M KCl electrode as the reference electrode and a platinum wire as the counter electrode. The deposited electrode films were used as the working electrodes (prepared by spin coating) in an electrolyte composed of a 0.06 M solution of $KClO_4$:ethanol in 1:1 volume ratio (under the same conditions as those used in the photocatalytic test). Electrochemical impedance spectroscopy (EIS) was performed at open circuit potential, under dark/blue-illumination conditions, using an AC perturbation of ± 25 mV. Blue illumination was performed using a compact xenon light source (Asahi Spectra, MAX-350), equipped with a blue emission filter ($\lambda = 450$ nm), where the optical fiber was placed in front of the film at 9 cm from the outside of the quartz cell. Finally, Mott Schottky plots and the space charge capacitance of the materials were measured under dark conditions at frequencies of 20, 40 and 60 Hz for the **CN1** and **CN2** materials and at 5, 10 and 20 Hz for **CS**, **CS/CN1-15** and **CS/CN2-10**. All electrochemical measurements were performed using a Gamry 600+ potentiostat.

Results and discussion

Crystalline structure

The XRD patterns of pure CdS and the composite samples with **CN1** and **CN2** are shown in Fig. 1a and b, respectively. The **CS** sample exhibited diffraction peaks corresponding to the (100), (002), (101), (102), (110), (103) and (112) planes, associated with the hexagonal (Wurtzite) phase of CdS (JCPDS No. 411049).^{29,32} For the polymerized **CN1** and **CN2** samples, two broad diffraction peaks at 2 theta values of 13° and 27° were observed, corresponding to the (100) and (002) planes, respectively, indexed to the tetragonal phase of $g-C_3N_4$ (JCPDS 87-1526).^{33,34} The (100) crystal plane of $g-C_3N_4$ is typically attributed to the internal structural unit of the triazine rings, whereas the (002) signal is attributed to the interplanar distance along the *c*-axis of $g-C_3N_4$, like in graphite. The difference in the (002) peak of the **CN1** and **CN2** materials suggests that hydrazine modifies the lamellar structure of $g-C_3N_4$. When 2 mL was used, the layers became compacted. This tendency is typically driven by the NH_3 atmosphere produced during hydrazine decomposition in the polymerization process.^{35–37}

The XRD pattern of the composite **CS/CN1-Y** samples, with $Y = 10, 15$ and 20 wt% (with **CN1**, Fig. 1a), showed the characteristic peaks of hexagonal-CdS. Despite the increased content of $g-C_3N_4$, the signals from the $g-C_3N_4$ samples were barely visible due to their relatively low concentration (Fig. 1a). However, the diffraction peak of the (002) plane of CdS appeared slightly shifted to a larger angle (marked with a dashed line), likely due to overlap with the (002) signal of the $g-C_3N_4-V_0$ support (at $\sim 27^\circ$ 2 θ , of **CN1**) reported in previous studies.^{10,38} Additionally, the broadening of the hexagonal CdS peaks in the composite samples suggests a reduction in crystal size below the equipment's detection limit of 4 nm. The reduced crystal size of the CdS material suggests that its growth may have been delayed by the presence of the dispersed **CN1** sample in the synthesis suspension. Similar to the composite samples with the **CN1** support, the XRD patterns of the composites with **CN2** (**CS/CN2-Y**, where $Y = 5, 10, 15$, and 20 wt%) exhibited the characteristic peaks of hexagonal CdS and the shifted (002) peak (Fig. 1b), confirming the overlap with the (002) interplanar signal of the **CN2** support. However, for the composite **CS/CN2-10** and **CS/CN2-15** samples, additional peaks at low angles ($10, 15$ and 18°) were detected. These peaks correspond to the orthorhombic structure of the $CdS(en)_{0.5}$ hybrid (Fig. S3†), typically observed when the synthesis reactions are conducted at low temperature (50 °C) or when the transformation toward pure CdS is incomplete.³⁹ The presence of the $CdS(en)_{0.5}$ hybrid in the **CS/CN2-10** and **CS/CN2-15** samples suggests that the transformation toward CdS was partially hindered by the presence of the dispersed **CN2** sample.

FT-IR analysis

The FT-IR spectra of hexagonal-CdS (**CS**), tetragonal $g-C_3N_4-V_0$ (**CNX**) and the composites **CS/CNX-Y** are displayed in Fig. 2.

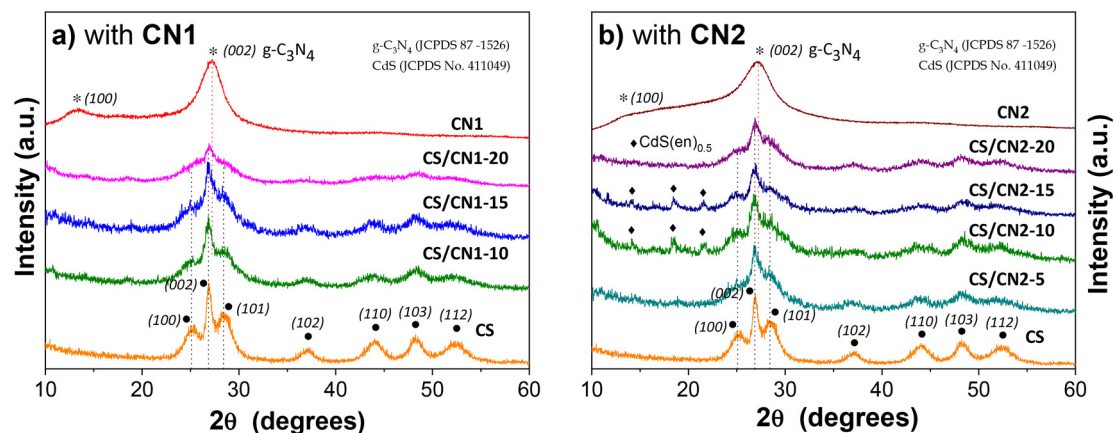


Fig. 1 XRD patterns of heterojunctions of CdS formed on g-C₃N₄ using the solvothermal method: (a) CN1 and (b) CN2 at different contents, along with pure CdS and g-C₃N₄.

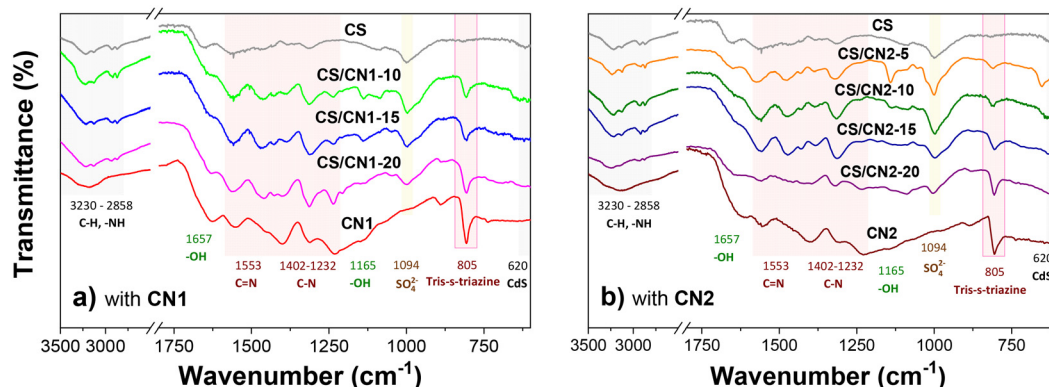


Fig. 2 FTIR analysis of heterojunctions of CdS formed on g-C₃N₄ (a) CN1 and (b) CN2 at different contents using the solvothermal method, along with pure CdS and g-C₃N₄.

The hexagonal-CdS sample exhibited absorption bands at 3230 and 3120 cm⁻¹ due to the stretching vibrations of the -NH and -NH₂ groups.^{29,40} It also exhibited two small bands at 2925 and 2858 cm⁻¹ related to C-H bond stretching vibrations, whereas the absorption band at 1310 cm⁻¹ is associated with the C-N bond. This set of functional groups is indicative of the presence of ENH⁺ bound to surface Cd²⁺ ions, with bands originating from the [Cd(ENH)₂]²⁺ complex, which are typically observed in hexagonal-CdS prepared in mixed solvents containing ethylenediamine. The absorption band at 1657 cm⁻¹ is attributed to the stretching vibrations of the hydroxyl bond (-OH) on the CdS surface.^{40,41} Finally, the absorption bands located at 1094 and 620 cm⁻¹ correspond to the stretching vibrations of the adsorbed sulfate group (SO₄²⁻) and the Cd-S bond, respectively.⁴² For the tetragonal g-C₃N₄ (CN1 and CN2 samples), wide peaks are observed at 3198 cm⁻¹, associated with the N-H stretching vibrations of the amino terminal groups. The stretching vibrations of the C-N aromatic heterocycles are observed at 1231, 1310 and 1402 cm⁻¹,⁴³ whereas the peaks at 1553 and 1631 cm⁻¹ are attributed to the stretch-

ing vibrations of the C=N bond.^{37,44} The peaks at 1425 and 1165 cm⁻¹ are related to the presence of -OH groups.⁴⁵ The intense absorption band at 805 cm⁻¹ is characteristic of the flexion mode of tris-s-triazine rings of polymerized g-C₃N₄ materials.^{46,47} For both composites with CN1 and CN2 (Fig. 2a and b, respectively), the absorption bands corresponding to -NH, -NH₂ (C-H) and C-N vibrations are clearly observed, indicating the presence of the [Cd(ENH)₂]²⁺ complex. However, the bands corresponding to the Cd-S (620 cm⁻¹) and SO₄²⁻ groups (1094 cm⁻¹) reduced as the content of tetragonal g-C₃N₄ was increased. Moreover, the bands at 1165 and 1425 cm⁻¹ (-OH groups) of hydroxylated g-C₃N₄ are also observed, and the 805 cm⁻¹ (Tris-s-triazine), 1231-1402 cm⁻¹ (C-N) and 1553 cm⁻¹ (C=N) bands^{44,46} indicate the presence of g-C₃N₄, becoming more evident when the content is increased to 20 wt%. The formation of the semiconductor heterojunction CdS/g-C₃N₄ is evidenced by the presence of Tris-s-triazine (see the rectangle in Fig. 2a and b), the [Cd(ENH)₂]²⁺ complex, and CdS vibrations bands, consistent with the information provided by the XRD analysis (Fig. 1).

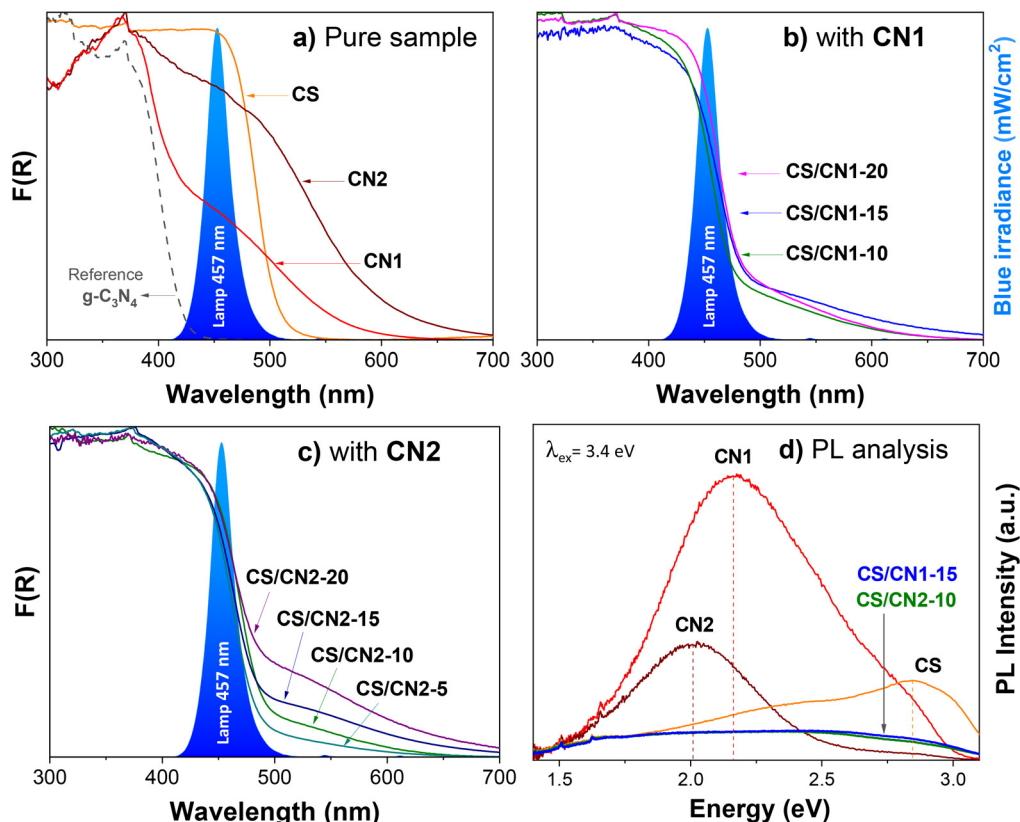


Fig. 3 DRS of (a) bulk CS, CN1 and CN2 and (b and c) composites with CN1 and with CN2, with the blue spectrum of the 455 nm LED lamp shown in the inset, and (d) PL characterization of bulk CS, CN1, CN2 and selected composites (CS/CN1-15 and CS/CN2-10).

Optical absorption and photoluminescence

In Fig. 3a, the UV-vis diffuse reflectance spectra of pure CS and CNX samples are displayed, along with the spectrum of $g-C_3N_4$ as a reference blank (prepared by polymerization of urea without adding hydrazine). The CS sample begins to absorb at ~ 525 nm, with an absorption maximum of ~ 475 nm in the visible light region. This blue absorption is related to the electronic transition of hexagonal-CdS. For both $g-C_3N_4-V_0$ (CN1 and CN2) samples, absorption maxima at ~ 370 nm and a broad shoulder between ~ 475 nm and ~ 675 nm are also observed. In comparison to reference $g-C_3N_4$, a more significant absorption is observed at the wavelength of interest (455 nm), and the expanded visible light absorption is likely due to structural defects within the $g-C_3N_4-V_0$ layers, particularly the presence of nitrogen vacancies (V_N). According to previous studies, these N vacancies may be promoted by the ammonia released from hydrazine during the polymerization process.²⁸ This effect is more evident for the $g-C_3N_4-V_0$ prepared in 2 mL of hydrazine (CN2 material), which exhibits a more extensive absorption range towards the visible spectrum. Using the Kubelka-Munk approximation and considering direct band transitions for CdS (linear graph $(FR \times hv)^2$ vs. hv , Fig. S4a†), the estimated band gap (E_g) for the CS sample is 2.50 eV, which agrees with that reported for the hexagonal-CdS

nanofibers.^{48,49} However, using indirect band transitions for $g-C_3N_4$ (Fig. S4c†), the estimated band gap (E_g) values for CN1 and CN2 are 2.00 and 1.80 eV, respectively. These values are consistent with expectations for modified $g-C_3N_4-V_0$ containing more structural defects.^{50–52}

Fig. 3b and c show the UV-vis diffuse reflectance spectra of all CS/CNX-Y composites. The samples exhibit an absorption maximum at 425 nm (denoted by the dotted line), which is shifted to high energies with respect to the bulk CS sample. In addition, they also exhibit expanded visible adsorption at ~ 675 nm, which must be related to the structural defects of the $g-C_3N_4-V_0$ layers. Considering that CdS is in major proportion in the composite, a direct band transition was used for the Kubelka-Munk approximation, and the estimated value of E_g for all the composites is in the range between 2.52 and 2.64 eV (Fig. S4a and b†). These E_g values are larger than those obtained for bulk CdS, which may be related to the quantum confinement effect of CdS. The quantum confinement effect occurs when the dimensions of CdS particles are comparable to the Bohr exciton diameter of CdS (< 5.8 nm).^{41,53} Moreover, the blue-shifted absorption might be related to the presence of the $CdS(en)_{0.5}$ hybrid, as suggested by XRD analysis, where CdS layers are separated by ethylenediamine, as reported.³⁹ The shaded area in Fig. 3a–c corresponds to the emission spectrum of the blue-LED lamp (455 nm), where it can be observed

that pure CdS, g-C₃N₄-V₀, and CS/CN_X-Y composites can absorb the blue light emitted by the LED lamp. This suggests that despite the blue-shifted absorption, all CS/CN_X-Y composites could be activated by blue light during the photocatalytic test. In Fig. 3d, the PL spectra of the bulk CS, CN1, CN2, and selected CS/CN1-15 and CS/CN2-10 composite materials are displayed. The optical excitation energy was 3.4 eV (~387.5 eV), at which all materials exhibited high light absorption. For CN1 and CN2 samples, an intense peak appears at 2.1 and 2.0 eV, respectively, likely due to a radiative e⁻/h⁺ recombination process. It is known that g-C₃N₄ typically exhibits a blue emission peak in its PL spectrum (around 2.59 eV) with a low-energy tail extending to 1.6 eV.⁵⁴ This emission is attributed to excitons generated within the s-heptazine rings. However, when N vacancies are present in g-C₃N₄, the PL emission peak is red-shifted,^{28,55} explaining the lower PL peak energies of CN1 and CN2. At the same time, the PL intensity of the CN2 sample is lower, suggesting a smaller fraction of radiative recombination than that of CN1. For the bulk CS, the PL spec-

trum exhibits a maximum emission in the blue region (at 2.88 eV) with a low-energy tail extending to 1.4 eV. The blue emission is attributed to transitions from the edge of the valence band to the conduction band.^{56–59} The PL spectra of the CS/CN1-15 and CS/CN2-10 heterojunctions are also shown in Fig. 3d. Considering that CdS is in major proportion in both composites, it can be noted that lower intensity in comparison with CS is observed, suggesting less radiative recombination, possibly due to better charge separation.^{59,60} The reduction in PL intensity appears to be independent of the amount of N vacancies in the g-C₃N₄ material.

Morphology and surface area

Fig. 4 displays the SEM images of the CS, CN1, and CS/CN1-15 samples. The CN1 material exhibits a lamellar morphology with lengths ranging from 2 to 10 μm and flake-like plates approximately 10 nm thick. This thickness creates significant spacing between the individual plates, attributed to low interplanar stacking along the *c*-axis of g-C₃N₄, as detected by XRD

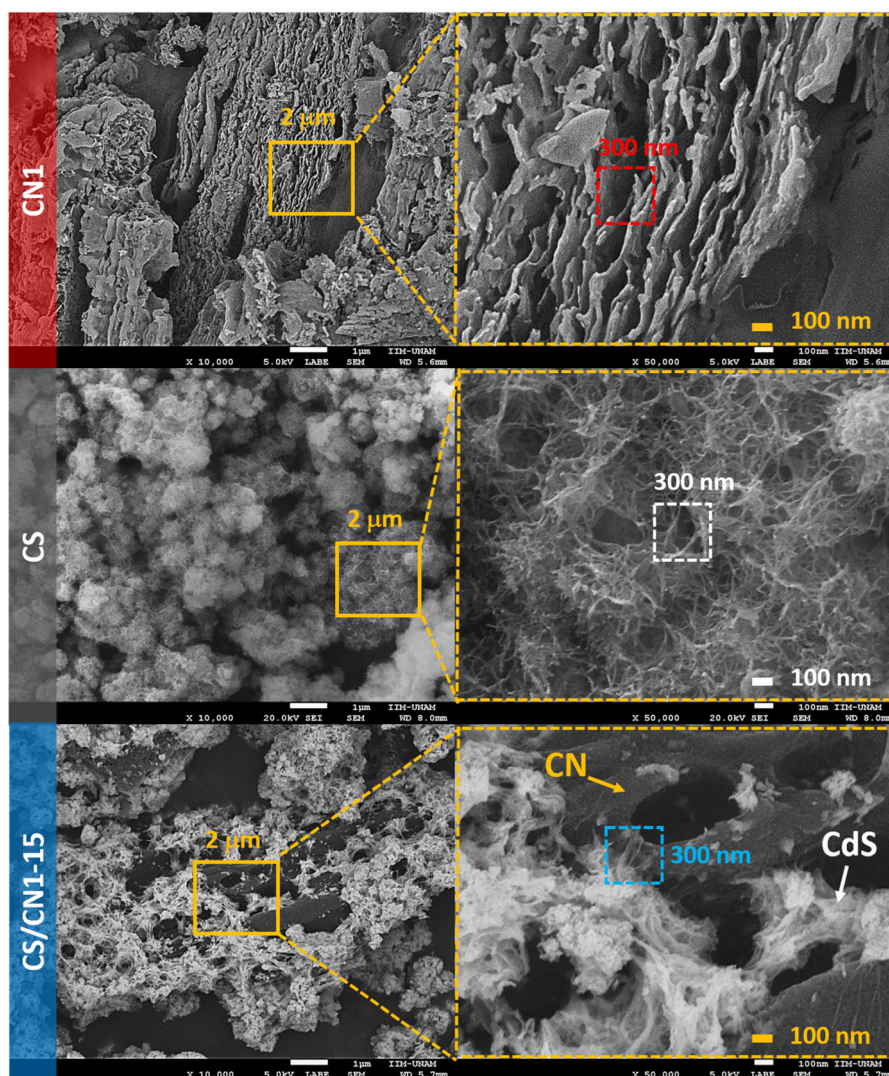


Fig. 4 SEM images of CN1, CS, and heterojunctions of CdS formed on g-C₃N₄ (CN1) at 15 wt% using the solvothermal method.

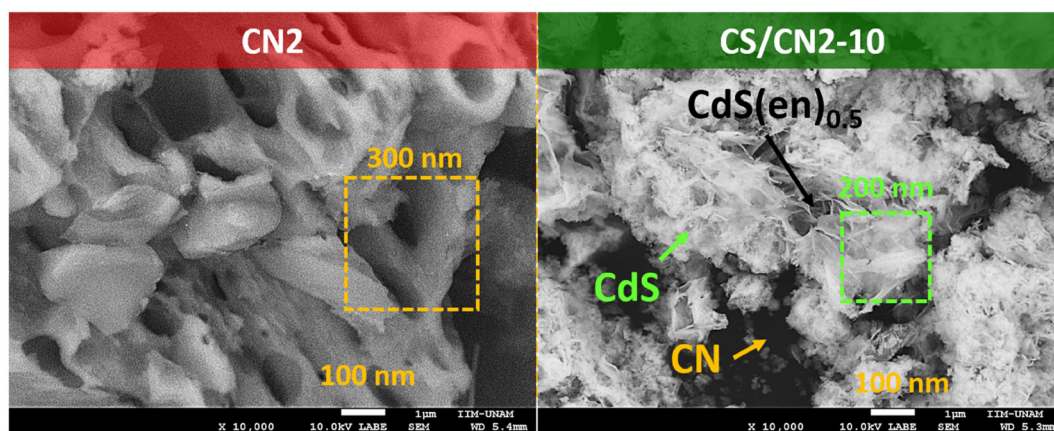


Fig. 5 SEM images of CN2 and heterojunctions of CdS formed on g-C₃N₄ (CN2) at 10 wt% using the solvothermal method.

(Fig. 2a). Consequently, the large particles (micro-flakes) composed of multiple thin plates lead to the formation of mesopores in the range of 50 to 150 nm. The SEM image shows that the hexagonal CdS material (CS) consists of fine nanofibers with diameters of 6 to 10 nm and lengths ranging from 100 to 250 nm. These nanofibers intertwine to form web-like agglomerates approximately 2 to 3 μm in size, with individual nanofibers remaining distinctly separated.

The SEM image of the CS/CN1-15 composites (Fig. 4) reveals extensive coverage of the CN1 micro-flakes by fine CdS nanofibers. These nanofibers range in length from 100 to 300 nm and in diameter from 1 to 10 nm, intertwining to form a web-like structure on the g-C₃N₄ surface. This intimate contact suggests an effective coupling between CdS and g-C₃N₄, confirming the success of the solvothermal method for the *in situ* growth of CdS on the thick plates of dispersed g-C₃N₄ in the solvent mixture (water : butanol : ethylenediamine). Similar fine nanofibers are observed for the CS/CN1-10 and CS/CN1-20 composites (not shown). While other researchers have reported various CdS morphologies, such as spheres, rods, or quantum dots on g-C₃N₄ surfaces, this work demonstrates the growth of fine CdS nanofibers on the thick plates of dispersed g-C₃N₄, using a butanol-aqueous solution for dispersion.

Fig. 5 presents the SEM images of the CN2 and CS/CN2-10 composite samples. The CN2 material displays a morphology of large micro-flakes with a layer thickness greater than that of the CN1 sample (~ 30 nm). These thicker layers result from the densification of the layered structure promoted by the loss of nitrogen due to the formation of NH₃ gas during the synthesis with a higher hydrazine concentration. This microstructure is consistent with the high interplanar (002) signal of CN2, detected by XRD (Fig. 2b). This compact morphology leads to minimal spacing between the individual layers, resulting in lower porosity. For the heterojunction formed using CN2 micro-flakes, the SEM image shows a dense network of fine nanofibers and thin layers around the compacted CN2 micro-flakes (at 10 wt%), resembling a spiderweb. As detected by

Table 2 Surface area data for heterojunctions with CN1 and CN2 samples

Sample with CN1	SA (m ² g ⁻¹)	E _g (eV)	Sample with CN2	SA (m ² g ⁻¹)	E _g (eV)
—	—	—	CS/CN2-5	84	2.52
CS/CN1-10	94	2.57	CS/CN2-10	79	2.56
CS/CN1-15	89	2.63	CS/CN2-15	71	2.58
CS/CN1-20	78	2.61	CS/CN2-20	63	2.64
CN1	39	2.00	CN2	17	1.80

The CS sample exhibited $S_g = 107$ (m² g⁻¹) and $E_g = 2.5$ (eV).

XRD, the fine nanofibers must be hexagonal-CdS, whereas the thin layers likely correspond to the CdS(en)_{0.5} hybrid. Similar morphologies were observed for other composites with varying contents of compact g-C₃N₄ micro-flakes (not shown), suggesting successful composite formation when CN2 is well-dispersed in a butanol-aqueous solution. The surface areas (SAs) for the CN1 and CN2 micro-flakes, and CS nanofibers are 39, 17, and 108 m² g⁻¹, respectively, consistent with the previously reported values.^{28,29} When the CS/CN1-Y composites are obtained, the surface areas are in the range of 94–78 m² g⁻¹, decreasing as the CN1 contents increase. The SAs for the CS/CN2-Y composites are further reduced to 84–63 m² g⁻¹, likely due to the lower porosity of the compacted lamellar CN2 (Table 2). The reduced SAs observed in both composites can be attributed to several factors: firstly, the minor proportion of CS nanofibers compared to the bulk CdS sample, which contributes less SA. Secondly, the compacted lamellar g-C₃N₄ (CN2) itself has an inherently lower SA than CN1. Thirdly, the contact area between CS and CNX, representing the inaccessible surface area, can also contribute to the overall decrease in the measured SA.

Blue irradiance in the composite suspensions

The blue light irradiance within the photoreactor system was characterized as a function of photocatalyst mass load (ranging from 5 to 20 mg in 200 mL, as shown in Fig. 6a).

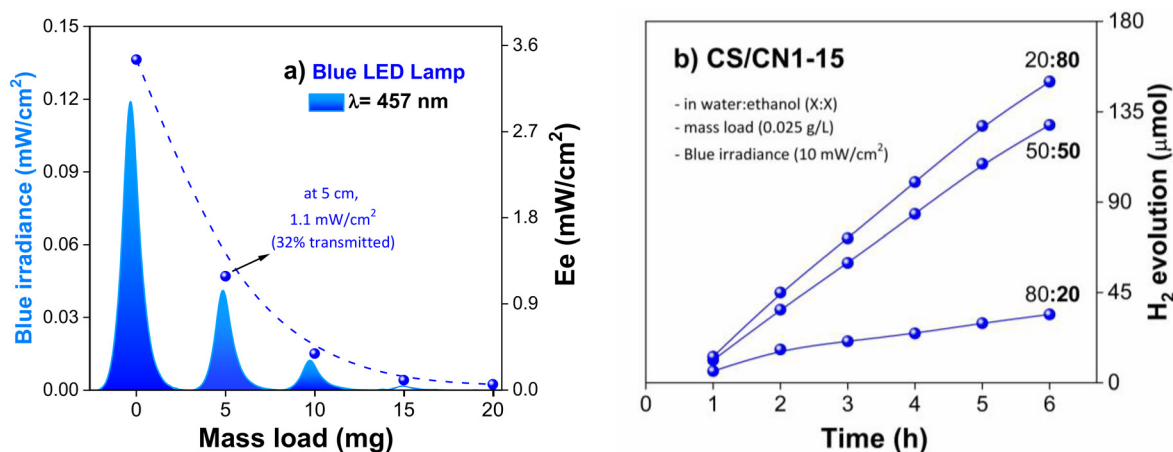


Fig. 6 Plot of blue irradiance measured inside the suspension as a function of the (a) mass load and (b) H_2 production profiles of CS/CNX-Y composite suspensions with varying ethanol : water volume ratios.

Using the well-dispersed photocatalyst suspension in an ethanol–water solution, the initial 3.5 mW cm^{-2} irradiance drastically decreased to 0.5 mW cm^{-2} as the photocatalyst mass load increased, likely due to light-scattering effects caused by the saturated CS/CNX-Y composite suspension. To achieve sufficient photocatalyst loading with high blue light penetration, minimize scattering effects, and maximize blue light absorption by the dispersed photocatalyst suspension, 5 mg of photocatalyst powder (equivalent to 0.025 g L^{-1}) was used. This optimal mass load was defined according to the registered 50% blue intensity (Fig. S2†), giving a $\lambda = 454 \text{ nm}$ and $I_0 = 1.1 \text{ mW cm}^{-2}$ from one LED lamp. Considering that the illumination was provided by 9 LED lamps, positioned 5 cm from the glass photoreactor, the total blue light intensity delivered was 10 mW cm^{-2} . Under these optimized conditions, H_2 production using the CS/CNX-Y composite was evaluated at three different ethanol-to-water volume ratios (Fig. 6b). With 20% ethanol, H_2 production reached $33.5 \mu\text{mol}$ in 6 hours, increasing significantly to $128.7 \mu\text{mol}$ with 50% ethanol and $150.1 \mu\text{mol}$ with 80% ethanol. However, the increase at 80% ethanol was only 16.6% higher than that at 50%, indicating diminishing returns at higher ethanol concentrations. Consequently, a 50:50 ethanol-to-water ratio was chosen for the photocatalytic evaluation of the materials.

Photocatalytic activity in H_2 production

The H_2 production from CN1 and CN2 micro-flakes under blue light is nearly negligible, similar to the photolysis reaction ($3 \mu\text{mol}$ in 6 h, Fig. S5†). Limited hydrogen production is expected from the ethanol:water mixture under blue light irradiation due to its relatively low energy (455 nm) and low intensity (10 mW cm^{-2}). Additionally, the blue light energy cannot be fully absorbed by the ethanol:water solution, and water splitting cannot be effectively achieved. Therefore, any amount of hydrogen detected in the well-dispersed photocatalyst suspension must be attributed to the reduction of protons when electron–hole pairs are photogenerated and sep-

arated by the photocatalyst, effectively inducing the reduction reaction. In the case of the modified $\text{g-C}_3\text{N}_4\text{-V}_0$, the extremely low hydrogen production suggests that neither the CN1 nor CN2 micro-flakes exhibit significant photocatalytic activity for water splitting despite their ability to absorb blue light. This negligible photoactivity may be attributed to the fast e^-/h^+ pair recombination rate or low exciton lifetime, as evidenced by PL analysis (Fig. 3d).

Fig. 7a and b displays the H_2 production profiles for the CS nanofibers and CS/CNX-Y composite photocatalysts as a function of irradiation time over 6 h. The CS nanofibers produced $85 \mu\text{mol}$ of hydrogen in 6 h, corresponding to a H_2 evolution reaction rate of $2.8 \text{ mmol h}^{-1} \text{ g}^{-1}$. When CdS nanofibers are grown on $\text{g-C}_3\text{N}_4$ micro-flakes to form CS/CNX-Y heterojunctions, hydrogen production improves compared to bulk CS nanofibers. This enhancement was most pronounced for the CS/CN1-15 and CS/CN2-10 photocatalysts, reaching HER rate values of 4.43 and $5.25 \text{ mmol h}^{-1} \text{ g}^{-1}$, respectively. These values exceeded those of other composites and bulk CS alone (Fig. 7b). The HER rates of the CS/CN1-15 and CS/CN2-10 heterojunctions were enhanced approximately 1.7 and 2.0 times, respectively, compared to bulk CS nanofibers. The formation of the heterojunctions and the synergistic effect of both materials were confirmed by testing H_2 production from physical mixtures of CS nanofibers with 15 wt% CN1 (CS+CN1-15) or 10 wt% CN2 (CS+CN2-10), as shown in Fig. 7a and b. It was observed that, for both physical mixtures, H_2 production was lower than that for the composites (CS/CN1-15 and CS/CN2-10). The hydrogen evolution reaction rates of 2.18 and $2.20 \text{ mmol h}^{-1} \text{ g}^{-1}$ for CS+CN1-15 and CS+CN2-10 were similar to those for CS nanofibers alone. This limited photoactivity in the physical mixtures is likely due to the lack of coupling between CdS and $\text{g-C}_3\text{N}_4$.

Cycles of stability and characterization

The heterojunction with the higher HER rate (CS/CN2-10) was evaluated over four cycles of reaction by using the same, blue-

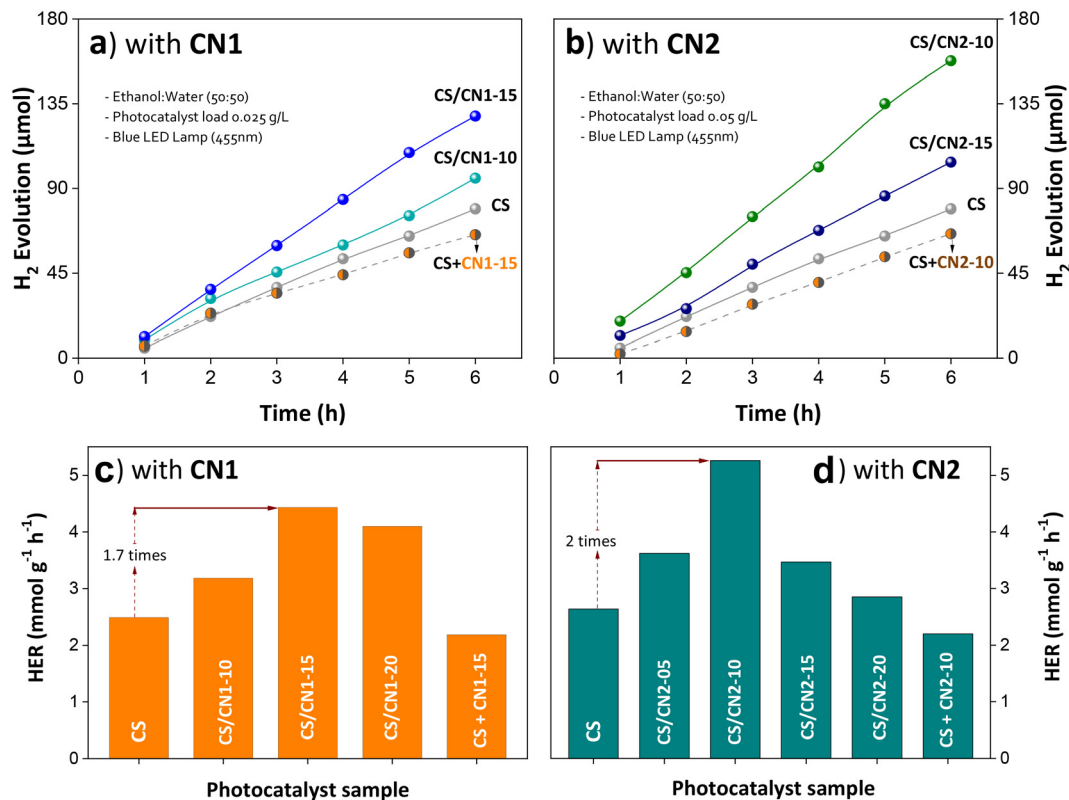


Fig. 7 Profile of H_2 production from ethanol : water solution using 0.025 g L^{-1} photocatalyst load, prepared (a) with CN1 samples and (b) with CN2 samples. (c and d) Profile of standardized H_2 production using composites with CN1 and CN2, respectively.

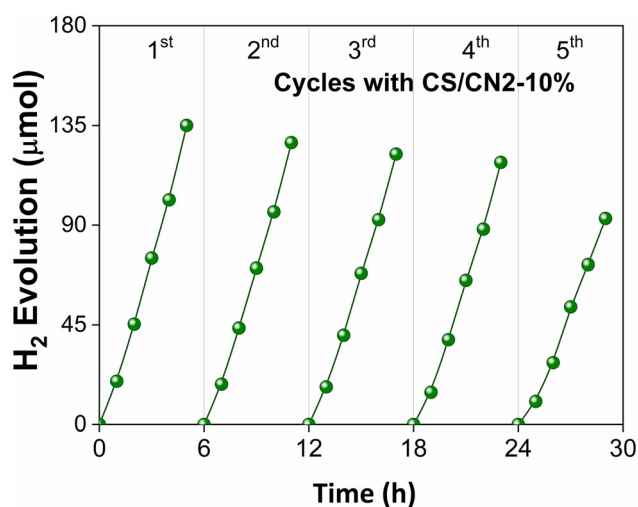


Fig. 8 Profile of H_2 production from ethanol : water solution using the CS/CN2-10 composite over four reaction cycles.

irradiated suspension (Fig. 8). It is observed that the H_2 production in the range of $4\text{--}5 \text{ mmol h}^{-1} \text{ g}^{-1}$ was maintained for at least three cycles of reaction; however, during the 4th cycle, the production slightly decreased. As mentioned in the literature, CdS/g- C_3N_4 composites typically exhibit HER rate values

ranging from 0.02 to $2.12 \text{ mmol h}^{-1} \text{ g}^{-1}$, often using high photocatalyst mass loads ($> 0.1 \text{ g L}^{-1}$) and intense Xe lamps (300 W , 150 mW cm^{-2}). In contrast, this work employed much lower mass loads (0.025 g L^{-1}) and lower light intensity (10 mW cm^{-2}) from blue LED lamps. Despite the less light intensity conditions, the CS/CN1-15 and CS/CN2-10 composites achieved significantly higher HER, comparable to those obtained when Pt is added to the reaction, highlighting their remarkable photoactivity.

The significant improvement in photoactivity observed for the CdS/g- C_3N_4 - V_0 composite suggests successful coupling between the two semiconductors, creating an internal electric field at their interface that reduces radiative recombination, regardless of the number of defects or the specific g- C_3N_4 - V_0 morphology. To further elucidate the mechanism responsible for the improved photocatalytic activity, additional experiments were conducted by photoelectrochemical (PEC) measurements, such as Mott-Schottky analysis and electrochemical impedance spectroscopy, which provide information about the charge transfer resistance at the semiconductor-electrolyte interface.

Considering that the amount of photocatalysts is extremely low (0.025 g L^{-1}), changes in the physicochemical properties of the reused composite could be expected. Therefore, to elucidate the cause of the detriment in photoactivity, additional XRD and FTIR characterization were performed for the recov-

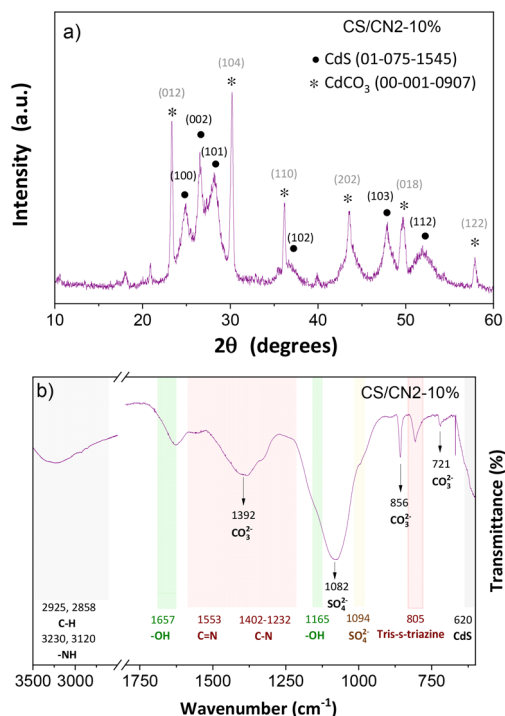


Fig. 9 (a) XRD patterns and (b) FTIR analysis of the used CS/CN2-10 composite after the 4th cycle of reaction.

ered CS/CN2-10 composite, after the 4th cycle of reaction. The XRD pattern of the used composites (Fig. 9a) showed the characteristic peaks for hexagonal-CdS; however, additional peaks emerged, which were associated with the crystalline phase of CdCO₃, as indexed by card-001-0907. Moreover, the signals from the g-C₃N₄ samples were barely visible due to the relatively low concentration, as previously mentioned. The formation of CdCO₃ was also evidenced by FTIR analysis (Fig. 9b), where the vibration peaks at 1392, 856, and 721 cm⁻¹ are related to the C=O vibrations corresponding to CO₃²⁻ groups.

The HRTEM images of the reused composites (Fig. 10) showed irregular microparticles covered with nanofibers, which are associated with C₃N₄ and CdS, respectively. In addition, elemental mapping analysis by using EDX coupled with HRTEM showed the presence of Cd, sulfur, carbon, and oxygen, which should be attributed to both CdS and CdCO₃. The observed changes in the physicochemical properties of the reused composite, attributed to the transformation of CdS into CdCO₃, are likely a consequence of the extremely low photocatalyst concentration (0.025 g L⁻¹) combined with high blue light penetration conditions. Conversely, employing higher photocatalyst concentrations (up to 0.1 g L⁻¹) could mitigate this effect, as the increased availability of photocatalyst would be expected to slow down the inherent transformation rate.

Photoelectrochemical properties

Electrochemical impedance spectroscopy (EIS, Fig. 11) was performed under dark and blue-light conditions using a KClO₄:

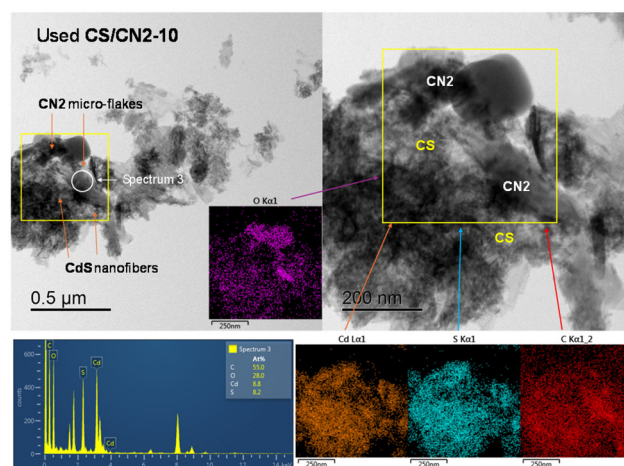


Fig. 10 HRTEM images and EDX mapping of the CS/CN2-10 composite.

water:ethanol electrolyte to assess the impact of coupling g-C₃N₄-V₀ with CdS nanofibers on charge transfer resistance. In the Nyquist impedance diagram, the charge transfer resistance is represented by the diameter of the semicircle, with a smaller diameter indicating more efficient separation of photogenerated electron-hole pairs, which correlates with improved photocatalytic performance. Blue light illumination of CN1 and CN2 films (Fig. 11a) shows minimal changes in their impedance response, indicating relatively high resistance to charge transfer, likely due to surface states acting as recombination centers. This observation aligns with the intense radiative recombination noted in their PL spectra (Fig. 3d). As a result, photocatalytic hydrogen production is scarcely achievable with CN1 or CN2 micro-flakes, as demonstrated by their negligible photoactivity (Fig. S5†). In contrast, the blue-illuminated CS film and the CS/CN1-15 and CS/CN2-10 composite films exhibit significantly smaller Nyquist semicircle diameters (Fig. 8b). This indicates a dramatic decrease in charge transfer resistance, suggesting efficient use of the photogenerated e⁻/h⁺ pairs and limited recombination. This finding aligns perfectly with the reduced radiative recombination observed in the PL spectra (Fig. 3d) for the heterojunctions. In addition, for the CS/CN2-10 electrode, the improved reduction in charge transfer resistance likely benefits further from thin CdS(en)_{0.5} hybrid layers detected by XRD and SEM (Fig. 5). The rapid carrier transfer process facilitates the swift movement of electrons to H⁺ ions, promoting H₂ formation and resulting in the observed high hydrogen production rate. This is directly correlated with the remarkable hydrogen evolution rates achieved by both CS/CN1-15 (4.43 mmol h⁻¹ g⁻¹) and CS/CN2-10 (5.25 mmol h⁻¹ g⁻¹) composites, underscoring their photoactivity compared to bulk CdS nanofibers or g-C₃N₄-V₀.

Mott-Schottky (MS) analysis (Fig. S6†) shows that the slopes of the MS plots are positive for the CN1 and CN2 materials, as well as for CS, CS/CN1-15, and CS/CN2-10, indicating the n-type character of the semiconductors.²²

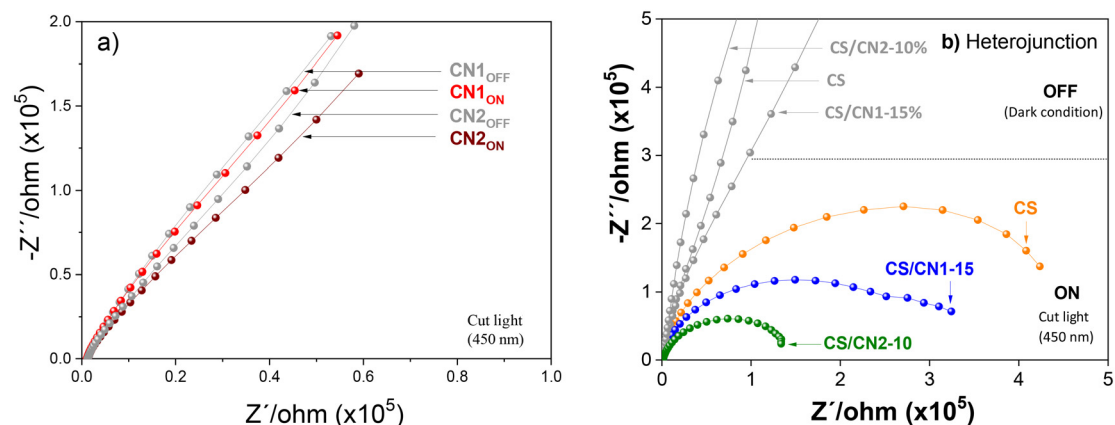


Fig. 11 (a) EIS of the CN1 and CN2 materials, (b) EIS of the CS, CS/CN1-15, and CS/CN2-10 materials under dark and light conditions.

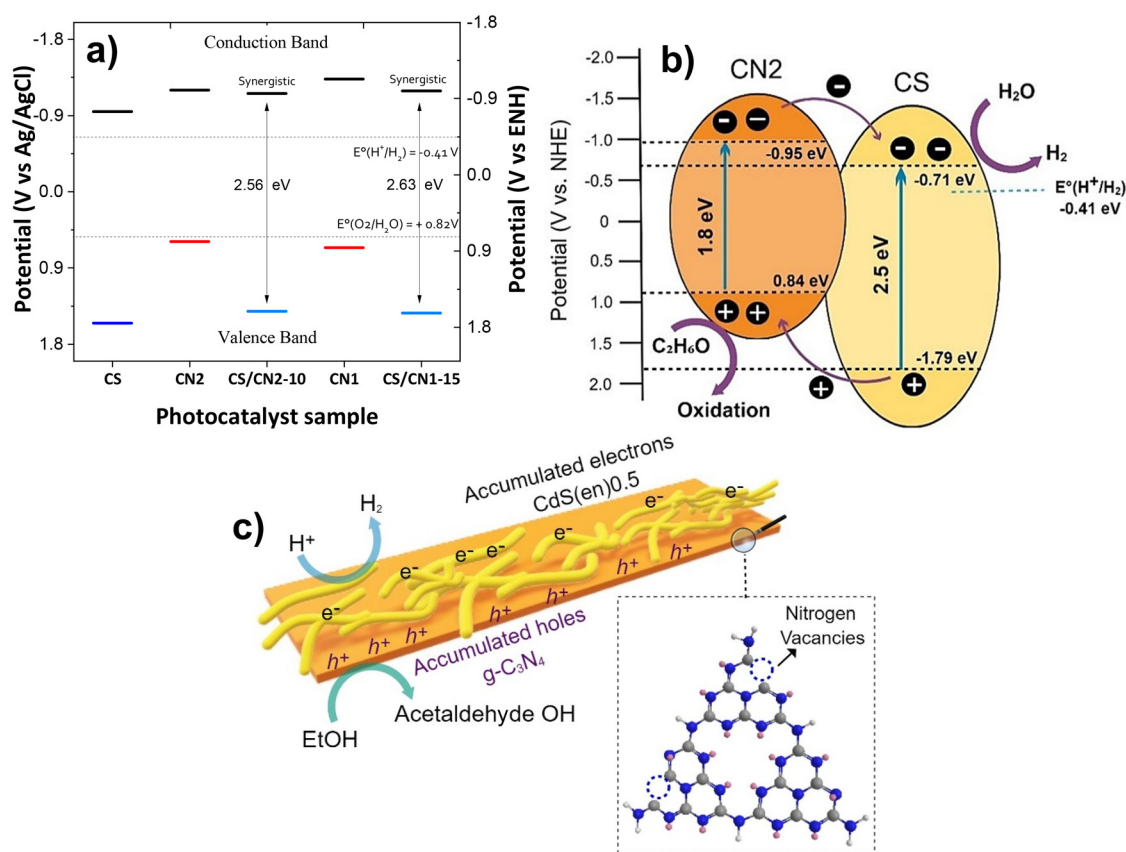


Fig. 12 (a) Band alignments for the materials estimated from the MS plot and band gap energy. (b) Mechanism of the synergistic effect of the CdS/g-C₃N₄ composite under blue-light irradiation. (c) Scheme illustrating the accumulation of electrons in CS nanofibers and holes in CN micro-flakes for H₂ production.

Extrapolation of the linear region in the MS plot at the three evaluated frequencies allows us to determine the flat band potential of the samples. Using the flat band potential and the optical band gap (Table 2), the minimum energy of the conduction band can be estimated for each material. The conduction band edges for the CN1, CN2, and CS materials are

approximately -1.33 , -1.20 , and -0.95 V vs. Ag/AgCl (-1.09 , -0.95 and -0.71 V vs. ENH), respectively (Fig. 12). On the other hand, the conduction band edge is similar for all composites, close to -1.19 and -1.16 V vs. Ag/AgCl (-0.99 and -0.96 V vs. ENH), respectively (Fig. 12). Compared to the bulk CS material, the composite's conduction and valence band edges

shifted very slightly, maintaining the energetic capacity to meet the redox potential requirements for H^+ reduction.^{3,48,61}

Synergistic effect of the coupled composite

Based on the experimental results, a mechanism for the synergistic effect of the $\text{CdS/g-C}_3\text{N}_4\text{-V}_0$ heterojunctions is proposed for photocatalytic H_2 production under blue-light irradiation. Fig. 12a illustrates the band edge positions of the components of CdS and $\text{g-C}_3\text{N}_4$. The valence band edges of **CN1** and **CN2** are close to $0.84 \text{ V} \pm 0.2 \text{ V}$ vs. ENH, while that of **CS** is significantly more positive (1.79 V vs. ENH). Considering that **CS** is in major proportion in the composites, the conduction band edge shifts slightly more negatively than that of CdS due to a new Fermi level equilibrium. Thus, the synergy between **CS** and $\text{g-C}_3\text{N}_4\text{-V}_0$ likely arises from factors like reduced recombination and improved electron transfer.

Upon blue light excitation (Fig. 12b):

- Electrons in both semiconductors are excited to their respective conduction bands.
- Electrons from the conduction band of $\text{g-C}_3\text{N}_4\text{-V}_0$ readily transfer to **CS** due to the “downhill” energy gradient, creating a built-in electric field due to the staggered band alignment.^{17,62}
- Holes from the valence band of **CS** simultaneously migrate to $\text{g-C}_3\text{N}_4\text{-V}_0$, minimizing the electron-hole recombination.

Electrons accumulated in **CS** nanofibers reduce H^+ ions to H_2 , while holes accumulated in $\text{g-C}_3\text{N}_4\text{-V}_0$ micro-flakes oxidize ethanol (Scheme in Fig. 12). The reduced radiative recombination observed in the PL spectra and the reduced charge transfer resistance observed in EIS studies support the proposed mechanism and explain the enhanced photocatalytic activity of $\text{CdS/g-C}_3\text{N}_4\text{-V}_0$.

Conclusions

In this study, we successfully prepared heterojunctions based on CdS nanofibers and defect-rich polymeric carbon nitride ($\text{g-C}_3\text{N}_4\text{-V}_0$) using standard fabrication techniques. Two $\text{g-C}_3\text{N}_4\text{-V}_0$ samples (**CN1** and **CN2**) with varying defect concentrations, likely nitrogen vacancies, were synthesized through hydrazine modification during urea polymerization. These defects enhanced the optical absorption of the materials, extending it into the visible and near-infrared range. Eight different heterojunctions were fabricated by combining CdS nanofibers (**CS**) with varying contents of **CN1** and **CN2** (5, 10, 15, and 20 wt%). The photocatalytic performance of these heterojunctions, along with the individual **CN1**, **CN2**, and **CS** samples, was evaluated for the hydrogen evolution reaction (HER) in an ethanol–water solution, without the use of Pt as a co-catalyst. A key innovation in this work was the optimization of reaction conditions, which demonstrated that efficient HER can be achieved using significantly lower photocatalyst mass (0.0125 g L^{-1}) and light irradiance (10 mW cm^{-2} , achievable with LEDs). Under these conditions, the best-performing het-

erjunctions, **CS/CN1-15** and **CS/CN2-10**, exhibited HER rates approximately 1.7 and 2.0 times higher, respectively, than bulk CdS nanofibers, achieving hydrogen production rates of 4.43 and $5.25 \text{ mmol h}^{-1} \text{ g}^{-1}$. This is double the performance reported for comparable CdS/ $\text{g-C}_3\text{N}_4$ heterojunctions in the literature. The superior performance of these heterojunctions can be attributed to several synergistic effects:

Enhanced light absorption

The combination of CdS nanofibers with **CN1** and **CN2** extends light absorption into the visible range, improving photocatalytic efficiency.

Efficient charge separation

The internal electric field at the $\text{CdS/g-C}_3\text{N}_4$ interface facilitates the separation of photogenerated electron–hole pairs, reducing recombination.

Reduced charge transfer resistance

The improved charge separation reduces charge transfer resistance, further boosting photocatalytic performance.

Because of these synergistic effects, the $\text{CdS/g-C}_3\text{N}_4$ heterojunction significantly outperformed physical mixtures of CdS and $\text{g-C}_3\text{N}_4$. Notably, the **CS/CN2-10** composite demonstrated consistently high HER activity over four cycles, indicating reduced radiative recombination.

Author contributions

Karen Valencia G.: conceptualization, investigation, methodology, formal analysis, and writing – original draft. Agileo Hernández-Gordillo: conceptualization, validation, and writing – review & editing. Lorena Cerezo: formal analysis. Sandra E. Rodil: resources, funding acquisition, supervision, project administration, and writing – review & editing.

Data availability

The authors confirm that the data that support the findings of this study are available within the article and its ESI.† The raw data supporting this study are available from the corresponding author [Agileo Hernández] upon reasonable request.

Conflicts of interest

There are no conflicts to declare.

Acknowledgements

Karen Valencia thanks CONACYHT México for the PhD scholarship. The authors acknowledge financial support from the PAPIIT-UNAM project IN112722. Finally, the authors gratefully recognize the support of Adriana Tejeda, Lourdes Bazan Díaz,

Alejandro Pompa, Diego Solis, and M. Angel Canseco for making the different measurements (LUME-SEM, XRD, PL, DRS, and FTIR analysis) possible.

References

- 1 A. Guterres, *The Sustainable Development Goals Report*, United Nations publication, 2023, pp. 1–80.
- 2 S. K. Lakhera, A. Rajan, T. P. Rugma and N. Bernaurdshaw, *Renewable Sustainable Energy Rev.*, 2021, **152**, 111694.
- 3 R. S. Mim, E. Sharaf Aldeen, A. Alhebshi and M. Tahir, *J. Phys. D: Appl. Phys.*, 2021, **54**, 503001.
- 4 H. Li, B. Cheng, J. Zhang, X. Zhou, C. Shi, L. Zeng and C. Wang, *J. Environ. Chem. Eng.*, 2023, **11**, 110371.
- 5 A. Gupta, B. Likozar, R. Jana, W. C. Chanu and M. K. Singh, *Int. J. Hydrogen Energy*, 2022, **47**, 33282–33307.
- 6 Z. Fiqar, J. Tao, T. Yang, Q. Liu, J. Hu and H. Tang, *Surf. Interfaces*, 2021, **26**, 101312.
- 7 S. Yilmaz, S. B. Törelı, M. Tomakin, İ. Polat and E. Bacaksız, *Phys. B*, 2025, **696**, 416622.
- 8 W. Li, W. Duan, G. Liao, F. Gao, Y. Wang, R. Cui, J. Zhao and C. Wang, *Nat. Commun.*, 2024, **15**, 6763.
- 9 W. Tang, L. Luo, Z. Fan, A. Zhang, Y. Ma, Y. Xie and J. Zhao, *Mater. Today Chem.*, 2024, **37**, 102000.
- 10 X. Chen, T. Hu, J. Zhang, C. Yang, K. Dai and C. Pan, *J. Alloys Compd.*, 2021, **863**, 158068.
- 11 T. Muhmood, I. Ahmad, Z. Haider, S. K. Haider, N. Shahzadi, A. Aftab, S. Ahmed and F. Ahmad, *Mater. Today Sustain.*, 2024, **25**, 100633.
- 12 S. R. Nagella, R. Vijitha, B. Ramesh Naidu, K. S. V. Krishna Rao, C.-S. Ha and K. Venkateswarlu, *Nano Energy*, 2023, **111**, 108402.
- 13 W. Li, X.-S. Chu, F. Wang, Y.-Y. Dang, X.-Y. Liu, X.-C. Wang and C.-Y. Wang, *Appl. Catal., B*, 2021, **288**, 120034.
- 14 S. Lv, H. Yuan, M. Xing, K. Li, Y. Leng Pak, X. Gao, D. Zhang, H. Mou and J. Song, *Chem. Eng. J.*, 2024, **492**, 152025.
- 15 Z. Fan, J. Huang, X. Huang, J. Li, Y. Xie, J. Liu, Y. Ling, W. Ye, Y. Ma and Y. Wang, *Sep. Purif. Technol.*, 2025, **359**, 130548.
- 16 Y. Niu, J. Shen, W. Guo, X. Zhu, L. Guo, Y. Wang and F. Li, *Molecules*, 2023, **28**, 6412.
- 17 J. Wang, R. Pan, Q. Hao, Y. Gao, J. Ye, Y. Wu and T. van Ree, *Appl. Surf. Sci.*, 2022, **599**, 153875.
- 18 H. Pang, Y. Jiang, W. Xiao, Y. Ding, C. Lu, Z. Liu, P. Zhang, H. Luo and W. Qin, *J. Alloys Compd.*, 2020, **839**, 155684.
- 19 J. Pan, P. Wang, P. Wang, Q. Yu, J. Wang, C. Song, Y. Zheng and C. Li, *Chem. Eng. J.*, 2021, **405**, 126622.
- 20 D. Ren, W. Zhang, Y. Ding, R. Shen, Z. Jiang, X. Lu and X. Li, *Sol. RRL*, 2019, **4**, 1900423.
- 21 J. Wang, Y. Fan, R. Pan, Q. Hao, J. Ye, Y. Wu and T. van Ree, *Nanoscale*, 2022, **14**, 7408–7417.
- 22 Y. Ran, Y. Cui, Y. Zhang, Y. Fang, W. Zhang, X. Yu, H. Lan and X. An, *Chem. Eng. J.*, 2022, **431**, 133348.
- 23 Y. Wang, X. Zhang, Y. Liu, Y. Zhao, C. Xie, Y. Song and P. Yang, *Int. J. Hydrogen Energy*, 2019, **44**, 30151–30159.
- 24 L. Chen, Y. Xu and B. Chen, *Appl. Catal., B*, 2019, **256**, 117848.
- 25 W. Wang, Y. Tao, L. Du, Z. Wei, Z. Yan, W. K. Chan, Z. Lian, R. Zhu, D. L. Phillips and G. Li, *Appl. Catal., B*, 2021, **282**, 119568.
- 26 W. Xue, W. Chang, X. Hu, J. Fan and E. Liu, *Chin. J. Catal.*, 2021, **42**, 152–163.
- 27 S. Du, L. Chen, C. Men, H. Ji, T. Su and Z. Qin, *J. Alloys Compd.*, 2023, **955**, 170265.
- 28 G. Valencia, A. Hernández-Gordillo, M. Méndez-Galván, D. Morett and S. E. Rodil, *Mater. Sci. Semicond. Process.*, 2022, **150**, 106900.
- 29 A. Hernández-Gordillo, A. B. Ramos, P. Acevedo-Peña, P. Jagdale, A. Tagliaferro and S. E. Rodil, *Catal. Today*, 2020, **341**, 59–70.
- 30 J. Liu, X. Wei, W. Sun, X. Guan and Z. Xiucheng, *Environ. Res.*, 2021, **197**, 111136.
- 31 L. Cerezo, K. Valencia G, A. Hernández-Gordillo, M. Bizarro, P. Acevedo-Peña and S. E. Rodil, *Int. J. Hydrogen Energy*, 2022, **47**, 22403–22414.
- 32 B. J. Huang, Y. Xie, B. Li, Y. Liu, Y. Qian and S. Zhang, *Adv. Mater.*, 2000, **12**, 808.
- 33 N. Meng, J. Ren, Y. Liu, Y. Huang, T. Petit and B. Zhang, *Energy Environ. Sci.*, 2018, **11**, 566–571.
- 34 S. Huang, Y. Zhao and R. Tang, *RSC Adv.*, 2016, **6**, 90887–90896.
- 35 X. Wu, X. Wang, F. Wang and H. Yu, *Appl. Catal., B*, 2019, **247**, 70–77.
- 36 R. Tejasvi and S. Basu, *Vacuum*, 2020, **171**, 108937.
- 37 K. Zhong, J. Feng, H. Gao, Y. Zhang and K. Lai, *J. Solid State Chem.*, 2019, **274**, 142–151.
- 38 J. Youa, W. Baoa, L. Wanga, A. Yanb and R. Guo, *J. Alloys Compd.*, 2021, **866**, 158921.
- 39 A. Hernández-Gordillo, A. G. Romero, F. Tzompantzi and R. Gómez, *Powder Technol.*, 2013, **250**, 97–102.
- 40 P. Dalvand, M. R. Mohammadi and D. J. Fray, *Mater. Lett.*, 2011, **65**, 1291–1294.
- 41 J. S. Roy, T. Pal Majumder and C. Schick, *J. Mol. Struct.*, 2015, **1088**, 95–100.
- 42 J. F. A. Oliveira, T. M. Milão, V. D. Araújo, M. L. Moreira, E. Longo and M. I. B. Bernardi, *J. Alloys Compd.*, 2011, **509**, 6880–6883.
- 43 F. Liu, T.-P. Nguyen, Q. Wang, F. Massuyeau, Y. Dan and L. Jiang, *Appl. Surf. Sci.*, 2019, **496**, 143653.
- 44 S. Zhang, Y. Liu, P. Gu, R. Ma, T. Wen, G. Zhao, L. Li, Y. Ai, C. Hu and X. Wang, *Appl. Catal., B*, 2019, **248**, 1–10.
- 45 W. Zhou, Z. Hu, F. Huang, W. Hong and X. Chen, *Appl. Catal., B*, 2020, **270**, 118852.
- 46 X. Du, G. Zou, Z. Wang and X. Wang, *Nanoscale*, 2015, **7**, 8701–8706.
- 47 R. Kumar, M. A. Barakat and F. A. Alseroury, *Sci. Rep.*, 2017, **7**, 12850.
- 48 G. Li, H. Liang, G. Xu, C. Li and J. Bai, *J. Phys. Chem. Solids*, 2020, **145**, 109549.

- 49 W. Ma, D. Zheng, Y. Xian, X. Hu, Q. Zhang, S. Wang, C. Cheng, J. Liu and P. Wang, *ChemCatChem*, 2021, **13**, 4403–4410.
- 50 S. Velmurugan, S. Balu, S. Palanisamy, T. C. K. Yang, V. Velusamy, S.-W. Chen and E.-S. I. El-Shafey, *Appl. Surf. Sci.*, 2020, **500**, 143991.
- 51 L. Meng, W. Yin, S. Wang, X. Wu, J. Hou, W. Yin, K. Feng, Y. S. Ok and X. Wang, *Chemosphere*, 2020, **239**, 124713.
- 52 I. Papailias, T. Giannakopoulou, N. Todorova, D. Demotikali, T. Vaimakis and C. Trapalis, *Appl. Surf. Sci.*, 2015, **358**, 278–286.
- 53 C. Bostedt, T. van Buuren, T. M. Willey, N. Franco, L. J. Terminello, C. Heske and T. Möller, *Appl. Phys. Lett.*, 2004, **84**, 4056–4058.
- 54 Y. Ding, C. Bo, L. X. Li, C. Gao, X. C. Ma, Z. Li and L. Yang, *Int. J. Hydrogen Energy*, 2024, **71**, 1373–1379.
- 55 B. Choudhury, K. K. Paul, D. Sanyal, A. Hazarika and P. K. Giri, *J. Phys. Chem. C*, 2018, **122**, 9209–9219.
- 56 K. Khurana and N. Jaggi, *J. Mater. Sci.: Mater. Electron.*, 2020, **31**, 10334–10346.
- 57 A. A. Sergeev, G. A. Naberezhnykh, V. A. Khomenko, A. V. Amosov, A. V. Nepomnyaschiy, T. F. Solov'eva, D. K. Chistyulin, M. V. Tutov, Y. N. Kulchin and O. D. Novikova, *Colloids Surf., B*, 2022, **217**, 112607.
- 58 V. Lahariya, E. Kumari and N. Singh, *Mater. Today: Proc.*, 2022, **48**, 622–625.
- 59 C. Yin, Y. Liu, X. Kang and X. Li, *Appl. Catal., A*, 2022, **636**, 118571.
- 60 K. A. Svit, A. A. Zarubanov, T. A. Duda, S. V. Trubina, V. V. Zvereva, E. V. Fedosenko and K. S. Zhuravlev, *Langmuir*, 2021, **37**, 5651–5658.
- 61 T. Goswami, H. Bhatt, D. K. Yadav and H. N. Ghosh, *J. Phys. Chem. B*, 2022, **126**, 572–580.
- 62 H. Gao, S. Zhang, J. Xu, Y. Dou, J. Zhou and R. Zhou, *J. Alloys Compd.*, 2020, **834**, 155201.